Smart Structures and Systems, *Vol. 31, No. 3 (2023) 213-227*
https://doi.org/10.12989/sss.2023.31.3.213

A novel prismatic-shaped isolation platform with tunable negative stiffness and enhanced quasi-zero stiffness effect

Jing Bian [1], Xuhong Zhou [1], Ke Ke*[1], Michael C.H. Yam [2], Yuhang Wang [1], Zi Gu [3] and Miaojun Sun [4,5]

[1] *School of Civil Engineering, Key Laboratory of New Technology for Construction of Cities in Mountain Area, Chongqing University, Chongqing, China*
[2] *Department of Building and Real Estate, Chinese National Engineering Research Centre for Steel Construction, The Hong Kong Polytechnic University, Hong Kong, China*
[3] *Department of Civil Engineering, Hunan University, Hunan, China*
[4] *Powerchina Huadong Engineering Corporation Limited, Hangzhou 310014, China*
[5] *Zhejiang Engineering Research Center of Marine Geotechnical Investigation Technology and Equipment, Hangzhou 310014, China*

(*Received July 10, 2022, Revised October 23, 2022, Accepted November 24, 2022*)

Abstract. A passive prismatic-shaped isolation platform (PIP) is proposed to realize enhanced quasi-zero stiffness (QZS) effect. The design concept uses a horizontal spring to produce a tunable negative stiffness and installs oblique springs inside the cells of the prismatic structure to provide a tunable positive stiffness. Therefore, the QZS effect can be achieved by combining the negative stiffness and the positive stiffness. To this aim, firstly, the mathematical modeling and the static analysis are conducted to demonstrate this idea and provide the design basis. Further, with the parametric study and the optimal design of the PIP, the enhanced QZS effect is achieved with widened QZS range and stable property. Moreover, the dynamic analysis is conducted to investigate the vibration isolation performance of the proposed PIP. The analysis results show that the widened QZS property can be achieved with the optimal designed structural parameters, and the proposed PIP has an excellent vibration isolation performance in the ultra-low frequency due to the enlarged QZS range. Compared with the traditional QZS isolator, the PIP shows better performance with a broader isolation frequency range and stable property under the large excitation amplitude.

Keywords: negative stiffness; quasi-zero stiffness; ultra-low frequency; vibration isolation

1. Introduction

In engineering practice, troublesome vibrations are inevitable, and vibration suppression is necessary. Among various vibration suppression methods, the passive vibration control methods were found to be promising solutions in engineering practice. The essence of the "passive vibration control" is similar to various seismic protection measures, and the structural nonlinear dynamic responsese can be controlled by modulating the nonlinear structural static and dynamic features (Du *et al*. 2020, Ke and Chen 2014, Ke and Yam 2016, Zhou *et al*. 2022a, b, c, Bian *et al*. 2022, Ren *et al*. 2023, Ke *et al*. 2023b, Zhang *et al*. 2023). Among various passive vibration control methods, the isolation platform is widely used due to its encouraging structural performance and practical attractiveness. For a linear stiffness isolation system, to achieve a wide isolation frequency range, the natural frequency of the isolation platform should be reduced, which leads to a decrease in the static loading capacity (Ibrahim 2008, Liu *et al*. 2015). To solve the above problem, nonlinear stiffness is planted in the isolation platforms. Quasi-zero stiffness (QZS) is a nonlinear stiffness that can achieve low stiffness near the equilibrium point without sacrificing the static loading capacity. Therefore, the design and the applications of QZS attracted much attention in recent years. Realizing that the composite action of composite members (Lai and Ho 2017, Ho *et al*. 2020, Lai *et al*. 2020, Ho *et al*. 2021, Yi *et al*. 2023) will affect the nonlinear dynamic behavior of the members, the QZS can be achieved by using composite material technologies (Liu *et al*. 2021, Zhong *et al*. 2019, Valeev *et al*. 2021, Mao and Saharabudhe 2006). By explicitly designing the configurations of novel composite materials (Guan *et al*. 2019, Wang *et al*. 2020b, c, 2022), the negative stiffness or QZS can be developed (Zhong *et al*. 2019, Liu *et al*. 2021).

Besides composite-material-based methods, the negative stiffness or QZS can be realized by structural-based technologies such as oblique springs (Gatti 2020, Hao and Cao 2015, Shaw *et al*. 2021, Wang *et al*. 2020a, Zhao *et al*. 2020, Kovacic *et al*. 2008, Carrella *et al*. 2012, Hao *et al*. 2017), buckled beams (Chen *et al*. 2021, Ding and Chen 2019, Duan *et al*. 2020, Liu *et al*. 2021), magnet springs (Li *et al*. 2021, Liu *et al*. 2021, Oyelade 2020, Wang *et al*. 2021, Xu *et al*. 2013, Zheng *et al*. 2018, Yang *et al*. 2021, Wu *et al*. 2014), cam-roller structures (Yao *et al*. 2020, Zou *et al*. 2021, Ye *et al*. 2020), bio-inspired structures (Wu *et al*. 2015, Bian and Jing 2019, 2020, 2021, Jing *et al*. 2021, Feng *et al*. 2019, Jing *et al*. 2019, Wang and Jing 2019, Yan

*Corresponding author, Research Professor,
E-mail: ke.ke@cqu.edu.cn
[a] Ph.D., E-mail: bian.jing@cqu.edu.cn

ISSN: 1738-1584 (Print), 1738-1991 (Online)

et al. 2022), and tower structures (Orlando and Goncalves 2013).

Recognizing the effectiveness of the QZS for vibration mitigations, researchers are actively pursuing novel isolation platforms with improved QZS characteristics such as enlarged QZS range,adjustable QZS property and multiple QZS, and stable QZS. For example, Gatti (2020) designed four oblique springs to achieve the QZS at large deflections. Hao and Cao (2015) developed a stable QZS with three springs and a flexible geometric arrangement. Shaw *et al*. (2021) used a combination of horizontal and vertical springs to realize the desirable QZS, and they examined the effectiveness of the novel platform in vibration suppression of a multi-mode-sensitive structure. Wang *et al*. (2020a) and Wang *et al*. (2021) developed a dual QZS mechanism to enhance the vibration suppression effect. Zhao *et al*. (2020) increased the QZS range by using two pairs of oblique springs. In these designs, oblique or horizontal springs were used to provide negative stiffness or QZS owing to the geometric nonlinearity of the isolation platform. In addition, the negative stiffness or QZS can be realized by buckling mechanisms of beams. For instance, Chen *et al*. (2021) designed vibration isolation joint with combined positive and negative stiffness by using buckling Euler beams. Ding and Chen (2019) studied the dynamic behavior of a slightly curved beam with a three-spring QZS isolator. Duan *et al*. (2020) reported the QZS property of a microgravity accelerometer with curved beams. Liu *et al*. (2021) installed buckled beams in horizontal direction to achieve the QZS for vibration isolation and energy harvesting. The magnet component can also be used to realize the QZS property. The magnetic forces in the opposite directions can offset the beam bending force (Li *et al*. 2021), the cable force (Liu *et al*. 2021), or the spring force (Oyelade 2020, Wang *et al*. 2021, Wang *et al*. (2020a), Xu *et al*. 2013, Zheng *et al*. 2018, Yang *et al*. 2021, Wu *et al*. 2014) to achieve the QZS effect. Moreover, the Cam-roller mechanism can be used to achieve the QZS (Yao *et al*. 2020, Zou *et al*. 2021) and the multiple QZS regions (Ye *et al*. 2020).

Recently, bio-inspired vibration isolation structures attracted much research attention owing to the tunable geometric nonlinearity and the beneficial QZS property. For instance, Jing and his co-workers (Wu *et al*. 2015, Bian and Jing 2019, 2021, Jing *et al*. 2021, Feng *et al*. 2019, Jing *et al*. 2019, Wang and Jing 2019) proposed a X-shaped structure or limb-like structure with nonlinear high-static-low-dynamic-stiffness and QZS. Yan *et al*. (2022) designed a toe-like structure to achieve enhanced vibration suppression in low frequency range. Deng *et al*. (2020) mimicked the multi-layer neck of a bird to achieve improved vibration isolation performance. Zhou and colleagues (Zhou *et al*. 2022a) proposed a bio-inspired X-shaped vibration isolation structure with the consideration of muscle contractile functions, joint friction and connecting rod mass simultaneously. Ling *et al*. (2022) designed a bio-inspired structure by mimicking the body structure of cockroaches for vibration isolation in low frequencies. Further, a group of enhanced QZS isolation platforms by utilizing the bio-inspired X-shaped mechanism were investigated by Chai *et al*. (2022). In summary, the bio-inspired structures show great potential in the flexible design of the nonlinear stiffness, including the negative stiffness and the QZS.

However, in previous studies (Wang and Jing 2019, Yao *et al*. 2020, Yan *et al*. 2022), the QZS range was limited or even unstable (followed by the negative stiffness), which could limit the moving range and the load-bearing. Therefore, there is still considerable space for the further improvement of the QZS property of the bio-inspired structures. In light of the above, this paper aimed to developing a prismatic-shaped isolation platform (PIP) to realize vibration isolation performance advances with tunable negative stiffness, enlarged QZS range, and improved stability. A tunable negative stiffness can be achieved by the installed horizontal spring. This negative stiffness mechanism mainly depends on the geometric nonlinearity in the motion process in the horizontal and vertical directions. The oblique springs are installed inside the prismatic structures, which can provide the positive stiffness. By combining and optimal designing these two kinds of stiffness, an enhanced QZS effect (stable with widen range) can be achieved. The concept of the platform is schematically shown in Fig. 1. A stable and widen QZS range can be obtained by combining the negative and positive stiffness rationally to achieve the enhanced vibration isolation performance (i.e., lower natural frequency, lower resonant peak and wider frequency range of vibration isolation). The novelty and main contributions of this paper is the proposed passive method which combines the negative stiffness and the positive stiffness in one compact isolation platform. The combined stiffness can be optimal designed to achieve the widen QZS range and stable loading-bearing capacity.

Note that the proposition is essentially a passive method to achieve the enhanced QZS effect based on structural geometric nonlinearity, which has great potential in practical engineering including the suspension system for the vehicle, vibration isolation for the civil structures, vibration isolation for precision instruments, vibration control of robot arms, etc.

The rest of this paper is organized as follows. In Section 2, the design concept of the PIP is discussed in detail, and its mathematical model is established. Then, the negative stiffness, the positive stiffness, the combined QZS effect, and the parameter influence are studied in Section 3. In Section 4, the dynamic analysis of the PIP is conducted, including the natural frequency, the displacement transmissibility, and the vibration isolation performance with the QZS effect. Finally, a conclusion is presented in Section 5.

2. Mathematical modeling

2.1 Notion of the prismatic-shaped structure

The negative stiffness effect due to the tension of the horizontal spring was studied in (Wu *et al*. 2015, Bian and Jing 2020, Jing *et al*. 2021), which might make the isolation platform unstable. Therefore, the negative stiffness is usually not used alone in the vibration isolation, as the

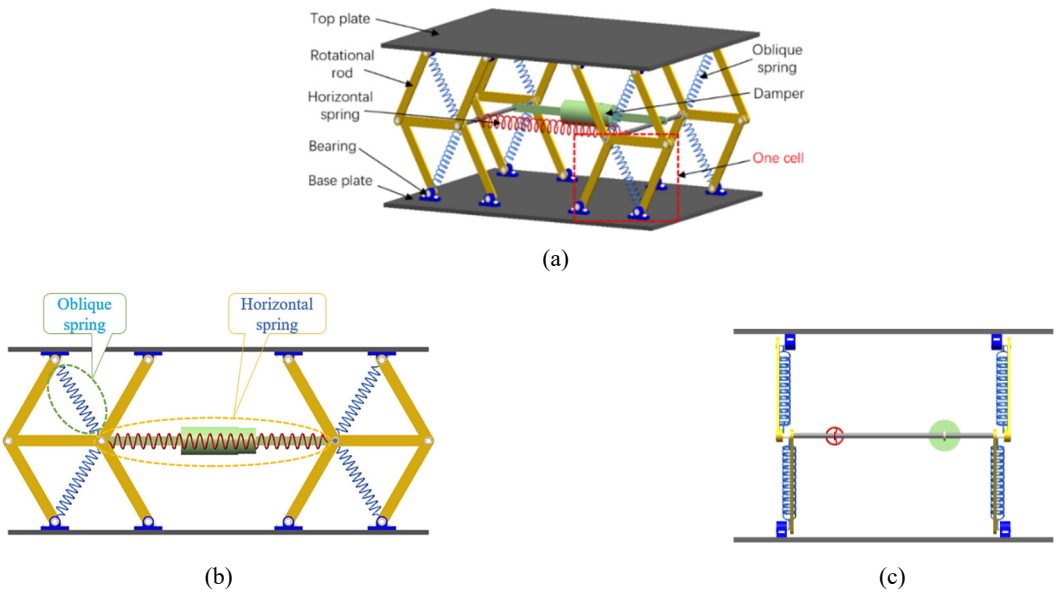

Fig. 1 The PIP: (a) notion of the PIP, (b) the front view and (c) the side view

structure should be supplemented by the positive stiffness to form the QZS and a stable isolation effect. Based on the above reasons, a prismatic-shaped isolation platform (PIP) with tunable negative stiffness and the positive stiffness is proposed in this paper. As shown in Fig. 1, a spring is horizontally installed in a prismatic structure, producing tunable negative stiffness at large deformations. The oblique springs installed inside the cell of the prismatic structure can produce a tunable positive stiffness. Therefore, by combining the negative stiffness and the positive stiffness, the tunable nonlinear quasi-zero stiffness (QZS) property can be achieved. Furthermore, the damper installed in the horizontal direction can achieve a geometrical nonlinear damping effect, which is displacement-dependent. The advantages of the geometrical nonlinear damping in the vibration isolation mainly are suppressing the amplitude peak in the resonance and maintaining low transmissibility in the higher frequencies. Thus, the horizontal damper can produce beneficially nonlinear displacement-dependent damping for the vibration isolation (Bian and Jing 2019). The main components of the PIP are labelled in Fig. 1(a). The rotational rods connect the top plate and the base plate by the bearings. In practical engineering, lightweight steel with advanced performance (Hua *et al*. 2022, Shi *et al*. 2022, 2023) that may survive hostile environment can be used to produce the rods. The excitation is transferred from the base plate. The mass (protected objective) is placed on the top plate. A spring and a damper are installed horizontally. The oblique spring is installed inside the cell of the PIP.

The concept of the combined QZS effect is displayed in Fig. 2. The combined effect of the negative stiffness from the horizontal spring and the positive stiffness from the oblique springs contributes to the QZS effect. The negative stiffness can be achieved by the horizontal spring when the whole platform is gradually compressed. The similar phenomenon is discovered in the previous studied (Wu *et al*. 2015, Bian and Jing 2020, Jing *et al*. 2021) with the

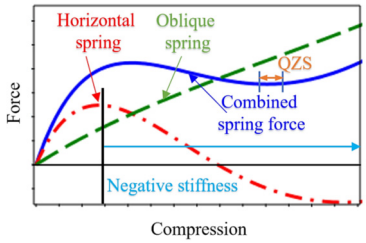

Fig. 2 Conceptual behavior of the PIP with tunable stiffness and the QZS effect

theoretical and experimental analysis. The force of the horizontal spring in the horizontal direction is positive, but the mapping of the spring force in the vertical direction could be positive, zero and negative as the compression process continues. In particular, the horizontal spring starts to show a negative stiffness when the PIP is deformed significantly under compression. By adding an additional positive stiffness, the stiffness of the entire structure can be modulated. As shown in Fig. 2, an increasing compression displacement results in increasing applied force in the horizontal spring as a clear indication of positive stiffness at the initial loading stage. With further displacement, the negative stiffness appears, which would lead to the collapse of the isolation platform. In contrast, the oblique springs always contribute to a positive stiffness of the platform. By combining the two kinds of springs, the overall force versus compression displacement response of the platform with an evident ascending branch in the equilibrium path can be characterized. Unlike the scenarios of seismic resistant structures that pursue a significant nonlinear stiffness ratio (Ke *et al*. 2023a, Chen and Ke 2019, Zhou *et al*. 2022c, Zhang *et al*. 2022), an enlarged QZS range is desirable toward an enhanced vibration isolation performance for the damper.

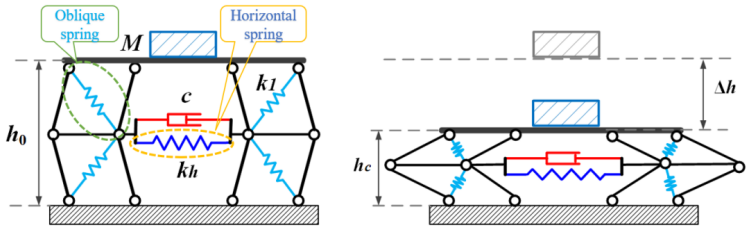

Fig. 3 Simplified model of the PIP

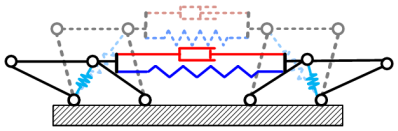

Fig. 4 Geometric deformation of one-layer of the prismatic-shaped structure

2.2 Deformation compatibility of the PIP

The simplified mechanical model of the PIP is displayed in Fig. 3. M is the loading mass, h_0 is the initial height of the PIP, k_h is the stiffness of the horizontal spring and k_1 is the stiffness of the oblique spring, c is the damping coefficient of the horizontal damper, Δh is the total displacement in the vertical direction, h_c is the height in the compression. Compression refers to the whole PIP in the compressing process. The geometric deformation of a one-layer of the PIP is shown in Fig. 4. Note that the PIP can have multiple layers for different applications, and a two-layer prismatic structure is chosen as an application example in the current study. In the compression, the horizontal spring and the damper are in the tension. The prismatic structure can keep the motion vertically and compress the oblique spring in the compression process.

Due to the symmetry, a single cell can be used to characterize half of a two-layer prismatic-shaped structure. Therefore, the displacement and the deformation compatibility of a single cell of the prismatic-shaped structure are displayed in Fig. 5. As shown in the figure, the motion can be in the negative direction and the positive direction along the y coordinate axis. L is the length of the rotational rod, l_0 is the initial length of the oblique spring and l_1 is the length of the oblique spring in the motion, Δx is the total displacement in the horizontal direction, θ is the initial angle and φ is the rotational angle in the motion. φ and Δh are positive when the rod rotates clockwise, whereas they are negative when the rod rotates counter-clockwise. The relationships of the motions in different directions are shown in Eqs. (1)-(3). Notably, φ and Δx have the nonlinear relationships with Δh which is the displacement in the vertical direction. Therefore, the relationship between horizontal and vertical motion is nonlinear. This mechanism achieves the geometric nonlinearity. All the structural parameters of the PIP used in the modeling are listed in Table 1. It is worth noting that the nonlinear behavior of the PIP would be entirely dependent on the geometric nonlinearity, and hence no hysteretic energy dissipation mechanisms (Chen and Bai 2021, Bai *et al*. 2022, He *et al*. 2022, Ke *et al*. 2023a, 2019a, Zhang *et al*. 2020, Zhou *et al*. 2021a, Li *et al*. 2022b, Lu *et al*. 2023) will be needed.

$$\varphi = \theta - arccos\left(cos(\theta) + \frac{\Delta h}{nL}\right) \tag{1}$$

$$x_1 = L(sin(\theta - \varphi) - sin(\theta)) \tag{2}$$

$$\Delta x = 2x_1 \tag{3}$$

The geometric relationships of the prismatic-shaped structure can be written as

$$l_0 = L\left(\sqrt{(\cos(\theta))^2 + (1 - \sin(\theta))^2}\right) \tag{4}$$

$$l_1 = L\left(\sqrt{(cos(\theta - \varphi))^2 + (1 - sin(\theta - \varphi))^2}\right) \tag{5}$$

$$\Delta l = l_1 - l_0 \tag{6}$$

2.3 Mathematic model of the PIP

The Lagrange principle is used herein for the dynamic modeling of the PIP. y denotes the coordinate of the mass M. The kinetic energy T of the isolation platform can be written as

$$T = \frac{1}{2}M\dot{y}^2 \tag{7}$$

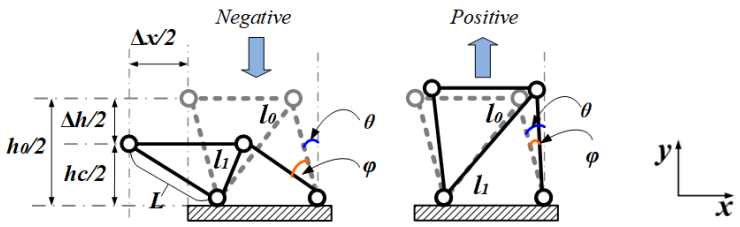

Fig. 5 The displacement of a single cell of the prismatic shaped structure

Table 1 The PIP structural parameters used in the modeling

Symbol	Structural parameters	Unit
M	Mass	kg
k_h	Horizontal spring stiffness	N m^{-1}
k_1	Oblique spring stiffness	N m^{-1}
c	Damping coefficient of the horizontal damper	N s m^{-1}
c_I	Damping coefficient of the air	N s m^{-1}
n	Number of layers v	-
L	Length of rod	m
l_0	Initial length of the oblique spring	m
l_1	Length of the oblique spring in the motion	m
Δh	Total displacement in the vertical direction	m
h_0	Initial height of the PIP	m
h_c	Height in the compression	m
θ	Initial angle of rod	rad
φ	Rotational angle	rad
Δx	Relative displacement between the two joints connecting the horizontal spring in horizontal direction	m
y_1	Relative displacement between the Mass and the foundation in vertical direction	m

where $\dot{(\cdot)} = d(\cdot)/dt$.

The velocity of the relative displacement ($\Delta\dot{x}$) can be expressed as

$$\Delta\dot{x} = (\partial\Delta x/\partial y_1)(\partial y_1/\partial t) \tag{8}$$

$$\Delta\dot{l} = (\partial\Delta l/\partial y_1)(\partial y_1/\partial t) \tag{9}$$

The potential energy V of the isolation platform can be written as

$$V = \frac{1}{2}k_h(\Delta x)^2 + 4\times\frac{1}{2}k_1(\Delta l)^2 \tag{10}$$

Considering the damping effect, a generalized force Q of the PIP with the non-constraint forces F_i along with the virtual displacements r_i can now be expressed as

$$\begin{aligned} Q &= \sum F_i\frac{\partial r_i}{\partial y_1} = -c\Delta\dot{x}\frac{\partial\Delta x}{\partial y_1} - c_1\dot{y}_1 \\ &= -c\dot{y}_1\left(\frac{\partial\Delta x}{\partial y_1}\right)^2 - c_1\dot{y}_1 \end{aligned} \tag{11}$$

where c is the damping coefficient of the horizontal damper and c_1 is the linear air damping coefficient.

The Lagrange's equation is presented here as

$$\frac{d}{dt}\left(\frac{\partial T}{\partial\dot{y}_1}\right) - \frac{\partial T}{\partial y_1} + \frac{\partial V}{\partial y_1} = Q \tag{12}$$

The term $\frac{\partial V}{\partial y_1}$ in Eq. (12) can be obtained as

$$\frac{\partial V}{\partial y_1} = \frac{\partial V}{\partial\Delta x}\frac{\partial\Delta x}{\partial y_1} + \frac{\partial V}{\partial\Delta l}\frac{\partial\Delta l}{\partial y_1} \tag{13}$$

Therefore, based on the Lagrange principle, the dynamic equation under the base excitation ($z_0 = A_0 cos\omega t$) can be obtained as

$$\begin{aligned} &M\ddot{y}_1 + c_1\dot{y}_1 + c\left(\frac{\partial\Delta x}{\partial y_1}\right)^2\dot{y}_1 + k_h\frac{\partial\Delta x}{\partial y_1}\Delta x + 4k_1\frac{\partial\Delta l}{\partial y_1}\Delta l \\ &= -M\ddot{z}_0 \end{aligned} \tag{14}$$

3. QZS effect

In this section, the QZS effect is examined. The horizontal spring force and the oblique spring force are obtained firstly. Based on the further parametric study, the desirable load carrying behavior of the PIP can be confirmed.

The stiffness force of the horizontal spring is obtained as

$$F_h = k_h\frac{\partial\Delta x}{\partial y_1}\Delta x \tag{15}$$

The force of the oblique springs inside the prismatic structure is written as

$$F_p = 4k_1\frac{\partial\Delta l}{\partial y_1}\Delta l \tag{16}$$

The combined nonlinear stiffness force is defined as

$$F_k = F_h + F_p \tag{17}$$

The critical displacement of the PIP in the vertical direction should be defined herein. When the PIP is compressed or stretched, the maximum values can be written as y_{m1} (maximum compression) and y_{m2}

(maximum tension), respectively.

$$y_{m1} = nL\cos(\theta) \tag{18}$$

$$y_{m2} = nL(1-\cos(\theta)) \tag{19}$$

3.1 Feasibility study of PIP with QZS

Fig. 6 displays the feasibility of the tunable, stable, and enlarged QZS of the proposed PIP in this study. The parameters are set as: $\theta = \pi/3$, $L = 0.1$, $k_h = 20000$. By utilizing the negative stiffness due to the horizontal spring and a suitable positive stiffness contributed by the oblique springs, the expected QZS can be seen, as shown in Fig. 6. The compression means the PIP is in the compression status, which means y_1 is negative. The value of the compression is measured from the initial position (θ) to the position ($\theta + \varphi$). When $k_1 = 0$, there is no oblique springs. In this case, the negative stiffness appears when y_1 is negative and its absolute value exceeds a certain value as shown in Fig. 6. When the absolute value of y_1 exceeds 0.014m, the negative stiffness appears ($\frac{\partial|F|}{\partial|y_1|} \leq 0$). By adding the positive stiffness produced by the oblique springs, the combined stiffness becomes tunable. For instance, in the case of $k_1 = 200$, in the whole compression process, the combined stiffness shows positive, negative, QZS and positive properties sequentially. In the case of $k_1 = 650$, an enlarged QZS range without the negative stiffness at large deformations can be achieved. As k_1 continues to increase (e.g., $k_1 = 900$), the combined stiffness only shows positive property without QZS in the whole compression process, which might not be ideal for vibration isolation. Therefore, the combination of $k_h = 2000$ and $k_1 = 650$ achieves the desired stiffness for the purpose of the vibration isolation. This result confirms the feasibility of the tunable, stable, and enlarged QZS by adding and designing the positive stiffness to offset the negative stiffness. It is also worth noting that the mechanical model of the PIP was developed based on the premise that the connections between the rods may be simplified by the pin idealization, which can be realized by minimizing the connection element size in the connections, e.g., end plates (Yam *et al*. 2019) or using hinges releasing moment (Yam *et al*. 2022). In addition, even though nonlinear behavior may be realized by the PIP, no inelastic damages will be sustained by the system owing to the elastic behavior of all elements. Thus, the platform is also self-centering (Hu *et al*. 2, 2022a, b, Hu and Wang 2021, Huang *et al*. 2020, 2022, Jin *et al*. 2022), which will deform to the original position upon unloading, and no additional re-centering force mechanism is required.

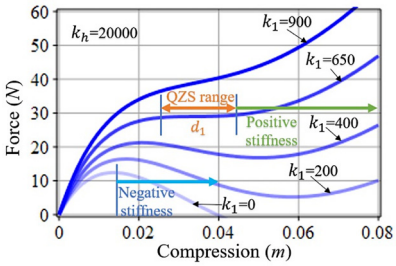

Fig. 6 Combined nonlinear stiffnesses with different k_1

3.2 Parametric study

3.2.1 Optimal stiffness with different initial angle (θ)

By tuning the system parameters, the behavior of the PIP can be optimized with widened QZS range. Two parameters, i.e., the initial angle (θ) and the rod length (L), affecting the QZS effect are further studied in this subsection. Based on the prototype platform discussed in the previous section, Figs. 7(a) and 7(b) shows the static response of the PIP with $\theta = \pi/4$ and $\theta = \pi/5$, respectively. As shown in Fig. 7(a), with an increase in k_1 (from 0 to 6000), the combined stiffness shows the negative stiffness, QZS, and positive stiffness sequentially. Notably, when $k_1 = 4500$, the widened QZS is achieved and followed by the positive stiffness, which means the stable QZS property. In this case, the width of the QZS (d_1) is 0.025 m. As shown in Fig. 7(b), the QZS can be achieved by tuning k_1 to 14000 when $\theta = \pi/5$ and $d_1 = 0.03$ m in this case. By comparing the results in Fig. 6 ($\theta = \pi/3$) and Fig. 7 ($\theta = \pi/4$ and $\theta = \pi/5$), decreasing the initial angel (θ) results in the increase in the width of the QZS.

3.2.2 Optimal stiffness with different rod length L

The optimal combined stiffness and the enlarged QZS can also be achieved with different L. Fig. 8(a) shows the combined stiffness by changing k_1 when $\theta = \pi/5$, L = 0.15 and $k_h = 20000$. The optimal combined stiffness is achieved with large range of QZS when $k_1 = 4500$. Moreover, with an increased L (e.g., L = 0.2), the optimal stiffness can be achieved by tuning k_1 to 4500 as shown in

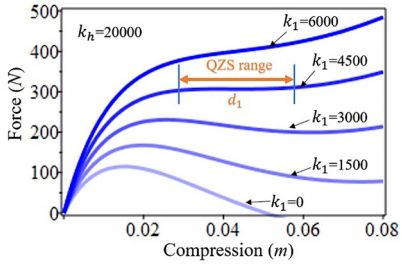

(a)

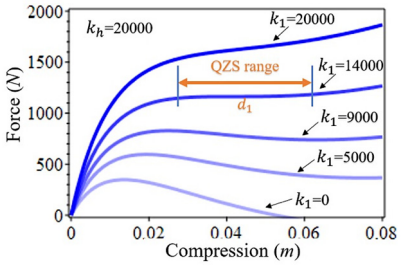

(b)

Fig. 7 Combined stiffness force when: (a) $\theta = \pi/4$ and (b) $\theta = \pi/5$

(a) (b)

Fig. 8 Combined stiffness force when: (a) $L = 0.15$ and (b) $L = 0.20$

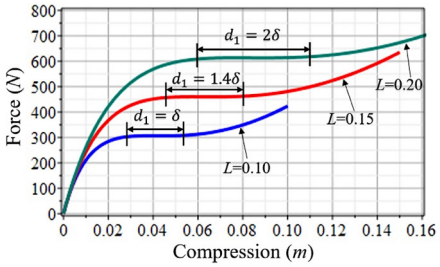

Fig. 9 QZS range with different L

Fig. 8(b). The same result can be seen in Fig. 7(a) when L = 0.1. Therefore, with different L, the optimal stiffness k_h and k_1 remain unchanged. The optimal stiffness $k_h = 20000$ and $k_1 = 4500$ when L = 0.10, L = 0.15 and L = 0.20. However, the range of the QZS is different with different L. The comparison result of the range of the QZS can be seen in Fig. 9. It is observed that an increasing L produces an increasing width of the QZS (d_1). Define $\delta = 0.025$ m, then d_1 increases from δ to $2\,\delta$ when L increases from 0.1 to 0.2. Therefore, we can increase the L to enlarge the width of the QZS.

4. Dynamic analysis

In this section, the dynamic performance of the PIP is analyzed. In addition, the parametric influence on the natural frequency of the PIP and the displacement transmissibility is explored.

4.1 Taylor expansion

Toward further solution of the second-order differential equation, the Taylor expansions are used to transfer the fractional functions (F_h, F_p, F_k and F_c) into the polynomial functions (f_h, f_p, f_k and f_c).

Thus, the stiffness force due to the horizontal spring (F_h) can be expanded as

$$f_h = k_h(\epsilon_1 y + \epsilon_2 y^2 + \epsilon_3 y^3 + \epsilon_4 y^4) \tag{20}$$

where the coefficients of the Taylor expansion are given as

$$\epsilon_1 = \frac{4}{n^2\, tan(\theta)^2} \tag{21}$$

$$\epsilon_2 = \frac{6\, cos(\theta)}{n^3 L\, sin(\theta)^4} \tag{22}$$

$$\epsilon_3 = \frac{2(4\, cos(\theta)^2 + 1)}{n^4 L^2 (1 - cos(\theta))^3 (1 + cos(\theta))^3} \tag{23}$$

$$\epsilon_4 = \frac{5\, cos(\theta)\,(4\, cos(\theta)^2 + 3)}{2n^5 L^3\, sin(\theta)^8} \tag{24}$$

The Taylor expansion of the stiffness force due to the oblique spring (F_p) can be obtained as

$$f_p = k_1(\eta_1 y + \eta_2 y^2 + \eta_3 y^3 + \eta_4 y^4) \tag{25}$$

where the coefficients of the Taylor expansion are given as

$$\eta_1 = \frac{2(1 + sin(\theta))}{n^2\, sin(\theta)^2} \tag{26}$$

$$\eta_2 = \frac{3\, cos(\theta)\,(2 + sin(\theta))}{2n^3 L (1 - cos(\theta))^2 (1 + cos(\theta))^2} \tag{27}$$

$$\eta_3 = \frac{5(3 + sin(\theta))\, cos(\theta)^2 + 3\, sin(\theta) + 5}{4n^4 L^2 (1 - cos(\theta))^3 (1 + cos(\theta))^3} \tag{28}$$

$$\eta_4 = \frac{cos(\theta)\,(35(4 + sin(\theta))\, cos(\theta)^2 + 65\, sin(\theta) + 140}{32n^5 L^3 (1 - cos(\theta))^4 (1 + cos(\theta))^4} \tag{29}$$

Thus, the total equivalent spring force (F_k) can be expanded as

$$f_k = (k_h\epsilon_1 + k_1\eta_1)y + (k_h\epsilon_2 + k_1\eta_2)y^2 + (k_h\epsilon_3 + k_1\eta_3)y^3 + (k_h\epsilon_4 + k_1\eta_4)y^4 \tag{30}$$

To demonstrate the accuracy of the Taylor expansion, representative comparison of the original expressions and the relative Taylor expansions in a broad spectrum of y_1 is displayed in Fig. 10. In this demonstration, the structural parameters are set as follows: $\theta = \pi/3$, $L = 0.15$, $n = 2$, $k_h = 20000$, $k_1 = 6500$ and c = 20. F_h is the original stiffness force of the horizontal spring and F_p is the original stiffness force of the oblique springs. F_k is the original total stiffness force. f_h, f_p and f_k are the Taylor expansions of the stiffness forces (Eq. (20), Eq. (25) and

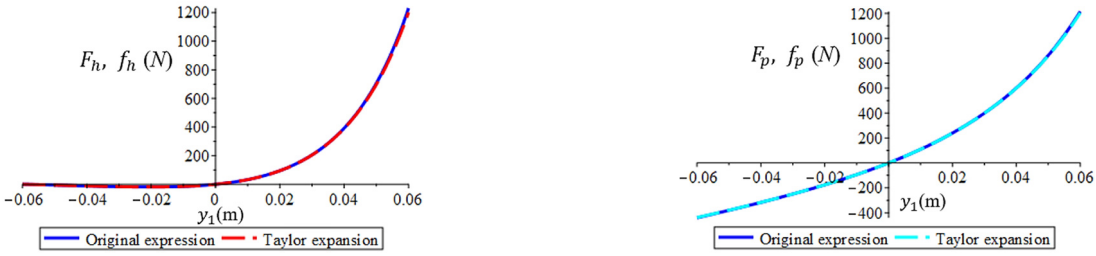

(a) (b)

Fig. 10 Comparison of the original term and the Taylor expansion: (a) horizontal spring stiffness force and (b) oblique spring stiffness force

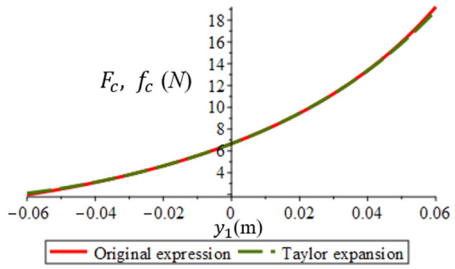

Fig. 11 Comparison of the original term and the Taylor expansion of the damping force

Eq. (30)). Fig. 10 compares the original stiffness forces and the Taylor expansions. In each figure, the curves match well, confirming the adequacy of the Taylor expansion in the given displacement range.

In addition, the damping force also needs the treatment for the further analysis. f_c is the Taylor expansion of the original damping force (F_c), which can be seen in Eq. (31). The coefficients of the Taylor expansion (f_c) is displayed in Eqs. (32)-(36). The comparison of the original damping force (F_c) and the Taylor expansion (f_c) is shown in Fig. 11. As shown in the figure, the accuracy of the Taylor expansion is verified.

$$f_c = c(\zeta_o + \zeta_1 y + \zeta_2 y^2 + \zeta_3 y^3 + \zeta_4 y^4) \tag{31}$$

$$\zeta_0 = \frac{4}{n^2\, tan(\theta)^2} \tag{32}$$

$$\zeta_1 = \frac{8\, cos(\theta)}{n^3 L\, sin(\theta)^4} \tag{33}$$

$$\zeta_2 = \frac{4(3\, cos(\theta)^2 + 1)}{n^4 L^2 (1 - cos(\theta))^3 (1 + cos(\theta))^3} \tag{34}$$

$$\zeta_3 = \frac{16\, cos(\theta)\, (cos(\theta)^2 + 1)}{n^5 L^3\, sin(\theta)^8} \tag{35}$$

$$\zeta_4 = \frac{4(5\, cos(\theta)^4 + 10\, cos(\theta)^2 + 1)}{n^6 L^4 (1 - cos(\theta))^5 (1 + cos(\theta))^5} \tag{36}$$

4.2 Dimensionless dynamic equation

With the Taylor expansion, the dynamic equation of the PIP can be written as

$$\begin{aligned} &M\ddot{y}_1 + c_1\dot{y}_1 + c(\zeta_o + \zeta_1 y + \zeta_2 y^2 + \zeta_3 y^3 + \zeta_4 y^4)\dot{y}_1 \\ &+(k_h\epsilon_1 + k_p\eta_1)y + (k_h\epsilon_2 + k_p\eta_2)y^2 + (k_h\epsilon_3 \\ &+k_p\eta_3)y^3 + (k_h\epsilon_4 + k_p\eta_4)y^4 = -M\ddot{z}_0 \end{aligned} \tag{37}$$

Introduce a dimensionless parameter α to define the stiffness ratio between the oblique spring and the horizontal spring.

$$\alpha = \frac{k_1}{k_h} \tag{38}$$

The natural frequency of the linear mass-spring system is defined as

$$\omega_1 = \sqrt{\frac{(1 + 4\alpha)k_h}{M}} \tag{39}$$

Dimensionless time is introduced as

$$\tau = \omega_1 t \tag{40}$$

The dimensionless excitation frequency (Ω) and the nonlinear equivalent damping ratio (ξ_c) are defined as

$$\Omega = \frac{\omega}{\omega_1} \tag{41}$$

$$\xi_c = \frac{f_c}{2M\omega_1} \tag{42}$$

Therefore, the dimensionless dynamic equation of the PIP under the base excitation ($z_0 = A_0 cos\omega t$) can be obtained as

$$\begin{aligned} &y_1'' + 2\xi_1 y_1' + 2\xi_c y_1' \\ &+\frac{1}{(1 + 4\alpha)}(\epsilon_1 y + \epsilon_2 y^2 + \epsilon_3 y^3 + \epsilon_4 y^4) \\ &+\frac{\alpha}{(1 + 4\alpha)}(\eta_1 y + \eta_2 y^2 + \eta_3 y^3 + \eta_4 y^4) \\ &-\Omega^2 A_0\, cos\, \Omega\tau = 0 \end{aligned} \tag{43}$$

where $(\cdot)' = d(\cdot)/d\tau$, A_0 is the excitation amplitude and $\xi_1 = c_1/2M\omega_1$ is the linear damping ratio. The symbols used in the dimensionless dynamic equation are listed in Table 2.

Table 2 The system parameters and variables in dynamic analysis

Symbol	System parameters	Unit
ω	Frequency of base excitation	rad s^{-1}
ω_1	Natural frequency of Mass-spring system	rad s^{-1}
z_0	Basement excitation in vertical direction	m
A_0	Amplitude of basement excitation	m
α	Stiffness ratio of k_1 and k_h	-
T_d	Displacement transmissibility in vertical direction	-
Ω	Dimensionless excitation frequency	-
τ	Dimensionless time	-
Ω_n	Dimensionless natural frequency	-
ξ_c	Equivalent nonlinear damping ratio	-
ξ_1	Linear damping ratio	-

4.3 Natural frequency

The dimensionless natural frequency of the PIP can be obtained as

$$\Omega_n = \sqrt{\frac{\epsilon_1 + \alpha\eta_1}{1+4\alpha}} = \sqrt{\frac{\frac{4}{n^2 tan(\theta)^2} + \frac{2\alpha(1+sin(\theta))}{n^2 sin(\theta)^2}}{1+4\alpha}} \quad (44)$$

In Eq. (44), ϵ_1 and η_1 are the coefficients of the linear component of the horizontal spring and the oblique spring, respectively. The dimensionless natural frequency (Ω_n) depends on the initial angle (θ) and the stiffness ratio (α). In this paper, the prismatic structure has two layers, which means $n = 2$. Therefore, only two parameters (θ and α) can affect Ω_n.

The influence of θ and α on Ω_n can be seen in Fig. 12(a). The parameters range are set as: $\alpha \in [0, 10]$, $\theta \in [0.5, 1.5]$. α is the stiffness ratio of k_1 and k_h. $\alpha = 0$ means no oblique spring stiffness. When $\alpha = 10$, the total oblique spring stiffness is forty times as much as the horizontal spring stiffness, which leads to a positive stiffness in the whole compression process. The range initial angle (θ) is $[0.5, 1.5]$ (approximately from $\pi/6$ to $\pi/2$) which are the critical angles of the prismatic structure in practice. Thus, the parameters range is chosen based on the feasibility of the QZS property and the structure property. In the figure, it is observed that a decreasing θ results in the increase in Ω_n. A decreasing α leads to an increasing Ω_n. Recalling that a smaller Ω_n is beneficial to the vibration isolation performance, this figure provides a design reference for the natural frequency of the isolation platform. The details of the contour lines of Ω_n is shown in Fig. 12(b). The value of Ω_n is labeled in each contour line.

In Fig. 13, several cases from the 3D figure in Fig. 12(a) are chosen to display the detailed influence of θ and α. It is worth noting that a trend reversal exists, which can be seen clearly in Fig. 13(a). A decreasing α results in the increase in Ω_n with small θ ($\theta < 1.05$), as θ increases to around 1.05, the trend reversal point appears. After this reversal point, a decreasing α results in the decrease in Ω_n. As shown in Fig. 13(b), an increasing θ leads to

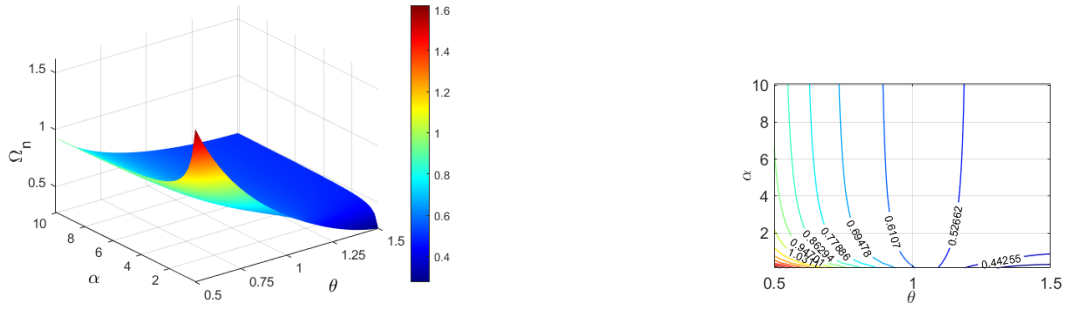

(a) (b)

Fig. 12 The dimensionless natural frequency Ω_n: (a) Ω_n with different θ and α and (b) the corresponding contour line of Ω_n

(a) (b)

Fig. 13 Dimensionless natural frequency Ω_n with: (a) different α and (b) different θ

a decreasing Ω_n. An increasing α also leads to the decrease in Ω_n without the trend reversal point.

4.4 Displacement transmissibility

By utilizing harmonic balance method (HBM), the first-order response of the system dynamic equation Eq. (43) can be assumed as

$$y_1 = Acos(\Omega\tau + \phi) \tag{45}$$

where A is the assumed amplitude of the motion, and ϕ is the assumed phase angle. By substituting Eq. (45) into Eq. (43), the unknown parameters can be obtained by solving a set of nonlinear algebraic equations for each excitation frequency (Ω) with the standard HBM procedure. The HBM transfers the differential equation into a set of algebraic equations. Therefore, the relationship between the system response and the input can be explored. Further theoretical or numerical analysis can be conducted based on the HBM. Substituting Eq. (45) into Eq (43), two algebraic equations are obtained

$$\begin{aligned}&[4(\gamma\epsilon_1 + \alpha\gamma\eta_1 - \Omega^2)\,cos(\phi) + 8\Omega\zeta_0\,sin(\phi)]A\\&+[2\Omega\zeta_2\,sin(\phi)^3 + 3\gamma(\alpha\eta_3 + \epsilon_3)\,sin(\phi)^2\,cos(\phi) + 2\Omega\zeta_2\,sin(\phi)\,cos(\phi)^2 + 3\gamma(\alpha\eta_3 + \epsilon_3)\,cos(\phi)^3]A^3\\&+[\Omega\zeta_4\,sin(\phi)^5 + 2\Omega\zeta_4\,sin(\phi)^3\,cos(\phi)^2 + \Omega\zeta_4\,sin(\phi)\,cos(\phi)^4]A^5 = 0\end{aligned} \tag{46a}$$

$$\begin{aligned}&[4(\gamma\epsilon_1 + \alpha\gamma\eta_1 - \Omega^2)\,sin(\phi) - 8\Omega\zeta_0\,cos(\phi)]A\\&+[3\gamma(\alpha\eta_3 + \epsilon_3)\,sin(\phi)^3 - 2\Omega\zeta_2\,sin(\phi)^2\,cos(\phi) + 3\gamma(\alpha\eta_3 + \epsilon_3)\,sin(\phi)\,cos(\phi)^2 - 2\Omega\zeta_2\,cos(\phi)^3]A^3\\&-[\Omega\zeta_4\,sin(\phi)^4\,cos(\phi) + 2\Omega\zeta_4\,sin(\phi)^2\,cos(\phi)^3 + +\Omega\zeta_4\,cos(\phi)^5]A^5 - 4\Omega^2A_0 = 0\end{aligned} \tag{46b}$$

The displacement transmissibility (T_d) of the PIP can be expressed as

$$\begin{aligned}T_d &= \frac{|A\,cos(\Omega\tau + \phi) + A_0\,cos(\Omega\tau)|}{|A_0\,cos(\Omega\tau)|}\\&= \frac{\sqrt{A^2 + A_0^2 + 2AA_0\,cos(\phi)}}{|A_0|}\end{aligned} \tag{47}$$

where $|\cdot|$ denotes to take the norm.

4.4.1 Parametric influence

The parametric influence on the displacement transmissibility of the PIP is displayed in Figs. 14 and 15. Without further explanation, the parameters are set as: $\theta = \pi/4$, $L = 0.2$, $k_h = 20000$, $\alpha = 1.5$, $c = 80$, $c_1 = 0$ and $A_0 = 0.03$. Fig. 14 studies the structural parametric influence on the displacement transmissibility (e.g., the initial angle (θ) and the rod length (L)). As shown in Fig. 14(a), an increasing θ results in a decreasing natural frequency, thus the resonant peak shifts to the left. Moreover, increasing θ leads to a decreasing damping effect, which increases the resonant amplitude. Therefore, more damping is needed to suppress the resonant amplitude as θ increases. In Fig. 14(b), the influence of rod length is displayed. An increasing L leads to increasing resonant amplitude due to the decreasing damping effect as L

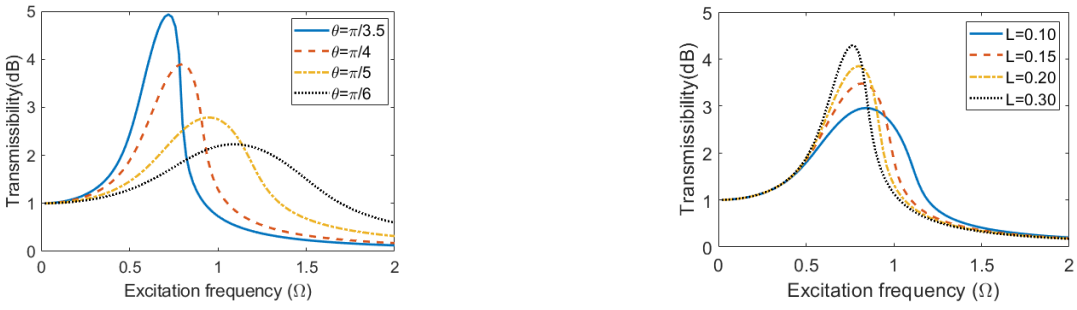

(a) (b)

Fig. 14 Displacement transmissibility with: (a) different θ and (b) different L

(a) (b)

Fig. 15 Displacement transmissibility with: (a) different α and (b) different c

(a) (b)

Fig. 16 Isolation performance with the QZS effect: (a) optimal static force with enlarged QZS range and (b) the transmissibility curves with different working positions

increases. From Eq. (44), the natural frequency is independent on L, therefore, changing L has no influence on the resonant frequency.

Fig. 15 studies the influence of the stiffness ratio (α) and the horizontal damping coefficient (c). As shown in Fig. 15(a), an increasing α results in a decreasing resonant frequency, which is consistent with the result shown in Fig. 13(b). Meanwhile, an increasing α leads to an increasing resonant amplitude, showing a slightly decreased damping effect. Fig. 15(b) displays the influence of the horizontal damping coefficient (c). Increasing c results in a decrease in the resonant amplitude, showing an increasing damping effect.

4.4.2 Isolation performance with the QZS effect

In the previous subsection, the structural parameters influence on the displacement transmissibility is studied. Further, the displacement transmissibility can be optimized with the QZS effect. From the static analysis result in Section 3, the enlarged QZS range can be achieved with the optimized combined spring stiffness. Thus, in this subsection, the isolation performance of the PIP with the enhanced QZS effect is studied.

Fig. 16(a) shows the optimized static force curve with a stable and enlarged QZS. The working position of the PIP can be optimally designed for the excellent vibration isolation performance based on the static force curve. For instance, the optimal working position is near $\frac{\partial F}{\partial y_1} = 0$ (QZS range). Mark four points in this force curve as A, B, C, and D, respectively. Notably, C and D locate in the QZS range. The information of the working position A, B, C and D is listed in Table 3. The specific working position demonstrated in in Fig. 16(a) can be achieved by tuning the angle (θ). In the design and assembly stage, the optimal working position can be decided based on the static force curve. Then by tuning the angle (θ), the specific working positions (e.g., A, B, C, D) can be achieved gradually.

To display the QZS effect for the dynamic property, the isolation performances in the four points are compared in Fig. 16(b) with the parameters setting as follows: $L = 0.2$, $k_h = 20000$, $k_1 = 650$, $c = 100$, $c_1 = 200$ and $A_0 = 0.02$. Fig. 16(b) shows the displacement transmissibility of the four working positions (A, B, C and D). The transmissibility peak gradually moves to the left with the reducing peak amplitude as the working position changes from A to D, which indicates the overall improvement of the vibration isolation performance. C and D locate in the QZS range as shown in Fig. 16(a), therefore, the isolation performance of the two points is improved compared with the performance of A and B. Notably, the PIP has the best vibration isolation performance at the working position D: lowest resonant frequency (widest isolation frequency range) and lowest resonant peak. The phenomenon verifies the excellent vibration isolation performance due to the QZS effect and the necessity of the enlarged QZS range. Without the oblique spring and the optimized stiffness, the QZS of the PIP is very limited (the point D doesn't exist) and the platform will collapse in significant amplitude movement due to the negative stiffness effect (unstable problem). Therefore, it is necessary to enlarge the QZS range for the excellent vibration isolation performance and the stability.

Table 3 Parameter of different working positions

Working position	Working angle (rad)	Compression length (m)
A	$\theta = 1.047$	0
B	$\theta = 1.104$	0.02
C	$\theta = 1.200$	0.055
D	$\theta = 1.253$	0.075

4.4.3 The excitation amplitude influence

For a linear isolator, the excitation amplitude has no influence on the displacement transmissibility. However, for a nonlinear system, the displacement transmissibility changes with different excitation amplitudes. The PIP is a nonlinear system with nonlinear stiffness and nonlinear damping. Therefore, the excitation amplitude can affect the transmissibility of the PIP and its influence on the transmissibility is studied in Fig. 17 with the excitation amplitude (A_0) increased from 0.01 m to 0.1 m. The parameters are set as: $\theta = 1.2$, $L = 0.2$, $k_h = 20000$, $\alpha = 0.00325$, $c = 500$ and $c_1 = 50$. The damper installed in the horizontal direction can achieve a geometrically nonlinear damping effect, which is displacement-dependent. When the displacement increases, the nonlinear damping effect is increased as well. As a result, with an increase in A_0 shown in Fig. 17, the resonant peak shifts to the right slightly, showing an enhanced nonlinear stiffness effect, and the resonant peak

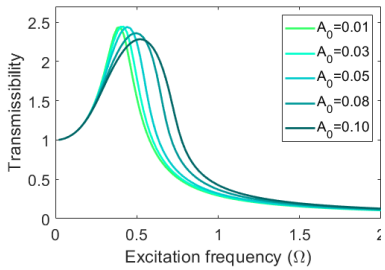

Fig. 17 Transmissibility with different excitation amplitude

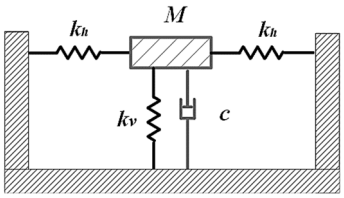

Fig. 18 Three-spring QZS isolator

decreases, showing an enhanced nonlinear damping effect. Therefore, the proposed PIP shows the stable performance with a large excitation amplitude. By contrast, the traditional three-spring QZS isolator may appear the strong nonlinear phenomena (e.g., bifurcation, instability, jump, and even chaos) as the excitation amplitude increases, which will be studied in the following subsection.

4.5 Comparison with benchmark QZS isolator

The configuration of the traditional QZS isolator with three-spring (Kovacic *et al*. 2008, Carrella *et al*. 2012, Hao and Cao 2015, Hao *et al*. 2017) and a linear damper is shown in Fig. 18. The general idea of the three-spring isolator becoming a QZS isolator is that using the horizontal springs to reduce the linear stiffness of the isolator k_v and to add an additional cubic nonlinear stiffness. QZS can be achieved when linear stiffness term is zero. It should be noticed that, not all three-spring isolators can achieve the QZS property, only those satisfying the previous requirements can be approximated by Duffing's equation with no linear stiffness term.

The dynamic dimensionless equation of the benchmark three-spring QZS isolator under base excitation can be approximated as a Duffing's equation

$$z_1'' + 2\xi_L z_1' + \mu z_1^3 = \Omega^2 A_0 \cos \Omega\tau \tag{48}$$

where ξ_L is the damping ratio and μ is the nonlinear stiffness ratio, which is defined as

$$\mu = k_h/k_v \tag{49}$$

The parameters of the PIP are the same as these used in Fig. 17 when $A_0 = 0.1$. Two nonlinear stiffness terms are obtained as: $\frac{1}{1+4\alpha} f_h = 0.1338y_1 + 1.5935y_1^2 + 6.4342y_1^3 + 19.3853y_1^4$ and $\frac{\alpha}{1+4\alpha} f_k = 0.0320y_1 + 0.0380y_1^2 + 0.1779y_1^3 + 0.4987y_1^4$. The nonlinear damping ratio is obtained as: $\xi_c = 0.0562 + 0.8928y_1 + 4.9417y_1^2 + 16.7299y_1^3 + 70.4469y_1^4$. The linear damping ratio is obtained as: $\xi_1 = 0.0372$, which can be easily achieved by a system composed of steel components (Ke *et al*. 2019b, Zhou *et al*. 2021a). In the benchmark three-spring QZS isolator, the linear damping ratio is set as: $\xi_L = 0.093$ which is same with the total linear damping of the PIP. The cubic stiffness ratio (μ) of the traditional QZS isolator is set as: $\mu = 6.61$, which is the same as the cubic component of the nonlinear stiffness of the PIP.

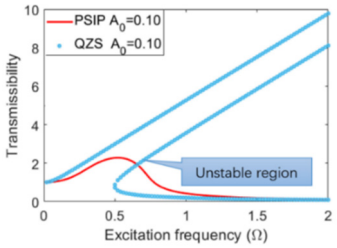

Fig. 19 Comparison of the PIP and the traditional QZS isolator

The comparison result is displayed in Fig. 19. The ordinate unit of this figure is linear dimensionless transmissibility. With the relatively large displacement excitation, the PIP can maintain stable vibration isolation performance with much lower resonant peak and wider isolation frequency range. By contrast, the traditional QZS isolator shows strong nonlinear properties, including the jump phenomenon and instability. The instability narrows down the isolation frequency range and leads to the safety problems, which needs to be avoided in the vibration isolation applications. Therefore, the proposed PIP shows enhanced vibration isolation performance with the insured stability, lower resonant peak, and wider isolation frequency range under the relatively large excitation amplitude.

5. Conclusions

In this paper, a novel isolation platform (PIP) is designed and analyzed. The proposed PIP shows beneficial nonlinearities, enlarged QZS range, adjustable resonant frequency, and stable property in a large vibration displacement. The enlarged QZS is achieved by combining the horizontal spring (negative stiffness) and the oblique spring (positive stiffness). With the optimal design, the PIP can achieve a stable and enlarged QZS effect. The main results and contributions are summarized as follows:

1. The negative stiffness, positive stiffness, and QZS effect can be achieved by combining the horizontal spring and the oblique spring installed inside the prismatic structure. The QZS effect can be improved with wider range with the optimal design.
2. With optimized stiffness ratio α, the QZS range can be enlarged with decreasing θ and increasing L.
3. The natural frequency of the PIP is designable and controllable. By tuning the initial angle (θ) and the stiffness ratio (α), the natural frequency can be

conveniently adjusted to achieve the ultra-low frequency isolation requirement. Specifically, by increasing the structural parameters θ and α, the natural frequency can be reduced.

4. Compared with the traditional three-spring QZS isolator, the proposed PIP can achieve a more stable QZS effect which is helpful to eliminate the potential instability, bifurcation, and jump phenomenon in the large vibration displacement.

Acknowledgments

This work was supported by the "Pioneer" and "Leading Goose" R&D Program of Zhejiang (Project Number: 2022C03009) and the National Natural Science Foundation of China (Grant No. 52178111 and 51890902).

References

Bai, J.L., He, J., Li, C., Jin, S.S. and Yang, H. (2022), "Experimental investigation on the seismic performance of a novel damage-control replaceable RC beam-to-column joint", *Eng. Struct.*, **267**, 114692. https://doi.org/10.1016/j.engstruct.2022.114692

Bian, J. and Jing, X.J. (2019), "Superior nonlinear passive damping characteristics of the bio-inspired limb-like or X-shaped structure", *Mech. Syst. Signal Process.*, **125**, 21-51. https://doi.org/10.1016/j.ymssp.2018.02.014

Bian, J. and Jing, X.J. (2020), "Analysis and design of a novel and compact X-structured vibration isolation mount (X-Mount) with wider quasi-zero-stiffness range", *Nonlinear Dyn.*, **101**(4), 2195-2222. https://doi.org/10.1007/s11071-020-05878-y

Bian, J. and Jing, X.J. (2021), "A nonlinear X-shaped structure based tuned mass damper with multi-variable optimization (X-absorber)", *Commun. Nonlinear Sci. Numer. Simul.*, **99**, 105829. https://doi.org/10.1016/j.cnsns.2021.105829

Bian, J., Zhou, X.H., Ke, K., Yam, M.C.H. and Wang, Y.H. (2022), "Seismic resilient steel substation with BI-TMDI: A theoretical model for optimal design", *J. Constr. Steel Res.*, **192**, 107233. https://doi.org/10.1016/j.jcsr.2022.107233

Carrella, A., Brennan, M.J., Waters, T.P. and Lopes, J.V. (2012), "Force and displacement transmissibility of a nonlinear isolator with high-static-low-dynamic-stiffness", *Int. J. Mech. Sci.*, **55**(1), 22-29. https://doi.org/10.1016/j.ijmecsci.2011.11.012

Chai, Y.Y., Jing, X.J. and Guo, Y.Q. (2022), "A compact X-shaped mechanism based 3-DOF anti-vibration unit with enhanced tunable QZS property", *Mech. Syst. Signal Process.*, **168**, 108651. https://doi.org/10.1016/j.ymssp.2021.108651

Chen, H. and Bai, J.L. (2021), "Seismic performance evaluation of buckling-restrained braced RC frames considering stiffness and strength requirements and low-cycle fatigue behaviors", *Eng. Struct.*, **239**, 112359. https://doi.org/10.1016/j.engstruct.2021.112359

Chen, Y. and Ke, K. (2019), "Seismic performance of high-strength-steel frame equipped with sacrificial beams of non-compact sections in energy dissipation bays", *Thin-Wall. Struct.*, **139**, 169-185. https://doi.org/10.1016/j.tws.2019.02.035

Chen, R.Z., Li, X.P., Yang, Z.M., Xu, J.C. and Yang, H.X. (2021), "A variable positive-negative stiffness joint with low frequency vibration isolation performance", *Measurement*, **185**, 110046. https://doi.org/10.1016/j.measurement.2021.110046

Deng, T.C., Wen, G.L., Ding, H., Lu, Z.Q. and Chen, L.Q. (2020), "A bio-inspired isolator based on characteristics of quasi-zero stiffness and bird multi-layer neck", *Mech. Syst. Signal Process.*, **145**, 106967. https://doi.org/10.1016/j.ymssp.2020.106967

Ding, H. and Chen, L.Q. (2019), "Nonlinear vibration of a slightly curved beam with quasi-zero-stiffness isolators", *Nonlinear Dyn.*, **95**(3), 2367-2382. https://doi.org/10.1007/s11071-018-4697-9

Du, K., Cheng, F., Bai, J.L. and Jin, S.S. (2020), "Seismic performance quantification of buckling-restrained braced RC frame structures under near-fault ground motions", *Eng. Struct.*, **211**, 110447. https://doi.org/10.1016/j.engstruct.2020.110447

Duan, Y.X., Wei, X.Y., Wang, H.R., Zhao, M.H., Ren, Z.M., Zhao, H.Y. and Ren, J. (2020), "Design and numerical performance analysis of a microgravity accelerometer with quasi-zero stiffness", *Smart Mater. Struct.*, **29**(7), 075018. https://doi.org/10.1088/1361-665X/ab8838

Feng, X., Jing, X.J., Xu, Z.D. and Guo, Y.Q. (2019), "Bio-inspired anti-vibration with nonlinear inertia coupling", *Mech. Syst. Signal Process.*, **124**, 562-595. https://doi.org/10.1016/j.ymssp.2019.02.001

Gatti, G. (2020), "Statics and dynamics of a nonlinear oscillator with quasi-zero stiffness behaviour for large deflections", *Commun. Nonlinear Sci. Numer. Simul.*, **83**, 105143. https://doi.org/10.1016/j.cnsns.2019.105143

Guan, M., Liu, W., Lai, M.H., Du, H., Cui, J. and Gan, Y. (2019), "Seismic behavior of innovative composite walls with high-strength manufactured sand concrete", *Eng. Struct.*, **195**, 182-199. https://doi.org/10.1016/j.engstruct.2019.05.096

Hao, Z.F. and Cao, Q.J. (2015), "The isolation characteristics of an archetypal dynamical model with stable-quasi-zero-stiffness", *J. Sound Vib.*, **340**, 61-79. https://doi.org/10.1016/j.jsv.2014.11.038

Hao, Z.F., Cao, Q.J. and Wiercigroch, M. (2017), "Nonlinear dynamics of the quasi-zero-stiffness SD oscillator based upon the local and global bifurcation analyses", *Nonlinear Dyn.*, **87**(2), 987-1014. https://doi.org/10.1007/s11071-016-3093-6

He, X., Chen, Y., Ke, K., Shao, T. and Yam, M.C.H. (2022), "Development of a connection equipped with fuse angles for steel moment resisting frames", *Eng. Struct.*, **265**, 114503. https://doi.org/10.1016/j.engstruct.2022.114503

Ho, J.C.M., Ou, X.L., Chen, M.T., Wang, Q. and Lai, M.H. (2020), "A path dependent constitutive model for CFFT column", *Eng. Struct.*, **210**, 210367. https://doi.org/10.1016/j.engstruct.2020.110367

Ho, J.C.M., Ou, X.L., Li, C.W., Song, W., Wang, Q. and Lai, M.H. (2021), "Uni-axial behaviour of expansive CFST and DSCFST stub columns", *Eng. Struct.*, **237**, 112193. https://doi.org/10.1016/j.engstruct.2021.112193

Hu, S.L. and Wang, W. (2021), "Seismic design and performance evaluation of low-rise steel buildings with self-centering energy-absorbing dual rocking core systems under far-field and near-fault ground motions", *J. Constr. Steel Res.*, **179**, 106545. https://doi.org/10.1016/j.jcsr.2021.106545

Hu, S.L., Wang, W. and Qu, B. (2020), "Seismic evaluation of low-rise steel building frames with self-centering energy-absorbing rigid cores designed using a force-based approach", *Eng. Struct.*, **204**, 110038. https://doi.org/10.1016/j.engstruct.2019.110038

Hu, S.L., Zhu, S.Y., Alam, M.S. and Wang, W. (2022a), "Machine learning-aided peak and residual displacement-based design method for enhancing seismic performance of steel moment-resisting frames by installing self-centering braces", *Eng. Struct.*, **271**, 114935. https://doi.org/10.1016/j.engstruct.2022.114935

Hu, S.L., Qiu, C.X. and Zhu, S. (2022b), "Machine learning-driven performance-based seismic design of hybrid self-centering braced frames with SMA braces and viscous dampers", *Smart Mater. Struct.*, **31**(10), 105024.

https://doi.org/10.1088/1361-665X/ac8efc
Hu, S.L., Wang, W., Alam, M.S. and Ke, K. (2023), "Life-cycle benefits estimation of self-centering building structures", *Eng. Struct.*, **284**, 115982. https://doi.org/10.1016/j.engstruct.2023.115982
Hua, J., Wang, F., Xue, X., Ding, Z. and Chen, Z. (2022), "Residual monotonic mechanical properties of bimetallic steel bar with fatigue damage", *J. Build. Eng.*, **55**, 104703. https://doi.org/10.1016/j.jobe.2022.104703
Huang, X.G., Zhou, Z., Eatherton, M.R., Zhu, D. and Guo, C. (2020), "Experimental investigation of self-centering beams for moment-resisting frames", *J. Struct. Eng.*, **146**(3), 04019214. https://doi.org/10.1061/(ASCE)ST.1943-541X.0002530
Huang, X.G., Liu, Y. and Sun, X. (2022), "Concept and analysis of resilient frictional shear connector for coupled system", *J. Build. Eng.*, **50**, 104172. https://doi.org/10.1016/j.jobe.2022.104172
Ibrahim, R.A. (2008), "Recent advances in nonlinear passive vibration isolators", *J. Sound Vib.*, **314**(3-5), 371-452. https://doi.org/10.1016/j.jsv.2008.01.014
Jin, S.S., Ai, P., Zhou, J. and Bai, J.L. (2022), "Seismic performance of an assembled self-centering buckling-restrained brace and its application in arch bridge structures", *J. Constr. Steel Res.*, **199**, 107600. https://doi.org/10.1016/j.jcsr.2022.107600
Jing, X.J., Zhang, L.L., Feng, X., Sun, B. and Li, Q.K. (2019), "A novel bio-inspired anti-vibration structure for operating hand-held jackhammers", *Mech. Syst. Signal Process.*, **118**, 317-339. https://doi.org/10.1016/j.ymssp.2018.09.004
Jing, X.J., Chai, Y.Y., Chao, X. and Bian, J. (2021), "In-situ adjustable nonlinear passive stiffness using X-shaped mechanisms", *Mech. Syst. Signal Process.*, **170**, 108267. https://doi.org/10.1016/j.ymssp.2021.108267
Ke, K. and Chen, Y. (2014), "Energy-based damage-control design of steel frames with steel slit walls", *Struct. Eng. Mech., Int. J.*, **52**(6), 1157-1176. https://doi.org/10.12989/sem.2014.52.6.1157
Ke, K. and Yam, M.C.H. (2016), "Energy-factor-based damagecontrol evaluation of steel MRF systems with fuses", *Steel Compos. Struct., Int. J.*, **22**(3), 589-611. http://doi.org/10.12989/scs.2016.22.3.589
Ke, K., Wang, W., Yam, M.C.H. and Deng, L. (2019a), "Residual displacement ratio demand of oscillators representing HSSF-EDBs subjected to near-fault earthquake ground motions", *Eng. Struct.*, **191**, 598-610. https://doi.org/10.1016/j.engstruct.2019.04.054
Ke, K., Wang, F., Yam, M.C.H., Deng, L. and He, Y. (2019b), "A multi-stage-based nonlinear static procedure for estimating seismic demands of steel MRFs equipped with steel slit walls", *Eng. Struct.*, **183**, 1091-1108. https://doi.org/10.1016/j.engstruct.2019.01.029
Ke, K., Yam, M.C., Zhang, P., Shi, Y., Li, Y. and Liu, S. (2023a), "Self-centring damper with multi-energy-dissipation mechanisms: Insights and structural seismic demand perspective", *J. Constr. Steel Res.*, **204**, 107837. https://doi.org/10.1016/j.jcsr.2023.107837
Ke, K., Chen, Y.H., Zhou, X.H., Yam, M.C.H. and Hu, S.L. (2023b), "Experimental and numerical study of a brace-type hybrid damper with steel slit plates enhanced by friction mechanism", *Thin-Wall. Struct.*, **182**, 110249. https://doi.org/10.1016/j.tws.2022.110249
Kovacic, I., Brennan, M.J. and Waters, T.P. (2008), "A study of a nonlinear vibration isolator with a quasi-zero stiffness characteristic", *J. Sound Vib.*, **315**(3), 700-711. https://doi.org/10.1016/j.jsv.2007.12.019
Lai, M.H. and Ho, J.C.M. (2017), "An analysis-based model for axially loaded circular CFST columns", *Thin-Wall. Struct.*, **119**, 770-781. https://doi.org/10.1016/j.tws.2017.07.024
Lai, M.H., Song, W., Ou, X.L., Chen, M.T., Wang, Q. and Ho, J.C.M. (2020), "A path dependent stress-strain model for concrete-filled-steel-tube column", *Eng. Struct.*, **211**, 110312. https://doi.org/10.1016/j.engstruct.2020.110312
Li, H.T., Ding, H., Jing, X.J., Qin, W.Y. and Chen, L.Q. (2021), "Improving the performance of a tri-stable energy harvester with a staircase-shaped potential well", *Mech. Syst. Signal Process.*, **159**, 107805. https://doi.org/10.1016/j.ymssp.2021.107805
Li, Y.W., Yam, M.C.H., Zhang, P., Ke, K. and Wang, Y.B. (2022), "Development of self-centring energy-dissipative rocking columns equipped with SMA tension braces", *Struct. Eng. Mech., Int. J.*, **82**(5), 611-628. https://doi.org/10.12989/sem.2022.82.5.611
Ling, P., Miao, L., Zhang, W., Wu, C. and Yan, B. (2022), "Cockroach-inspired structure for low-frequency vibration isolation", *Mech. Syst. Signal Process.*, **171**, 108955. https://doi.org/10.1016/j.ymssp.2022.108955
Liu, C.C., Jing, X.J., Daley, S. and Li, F.M. (2015), "Recent advances in micro-vibration isolation", *Mech. Syst. Signal Process.*, **56**, 55-80. https://doi.org/10.1016/j.ymssp.2014.10.007
Liu, C.R., Zhao, R., Yu, K.P., Lee, H.P. and Liao, B.P. (2021), "A quasi-zero-stiffness device capable of vibration isolation and energy harvesting using piezoelectric buckled beams", *Energy*, **233**, 121146.
Lu, Y., Liu, Y., Wang, Y., Liu, J. and Huang, X.G. (2023), "Development of a novel buckling-restrained damper with additional friction energy dissipation: Component tests and structural verification", *Eng. Struct.*, **274**, 115188. https://doi.org/10.1016/j.engstruct.2022.115188
Mao, Y. and Saharabudhe, S. (2006), "Nonlinear, seismic response spectra of smart sliding isolated structures with independently variable MR dampers and variable stiffness SAVS system", *Struct. Eng. Mech., Int. J.*, **24**(3), 375-393. https://doi.org/10.12989/sem.2006.24.3.375
Orlando, D. and Goncalves, P.B. (2013), "Hybrid nonlinear control of a tall tower with a pendulum absorber", *Struct. Eng. Mech., Int. J.*, **46**(2), 153-177. https://doi.org/10.12989/sem.2013.46.2.153
Oyelade, A.O. (2020), "Experiment study on nonlinear oscillator containing magnetic spring with negative stiffness", *Int. J. Non-Linear Mech.*, **120**, 103396. https://doi.org/10.1016/j.ijnonlinmec.2019.103396
Ren, F.M., Tian, S.Y., Gong, L., Wu, J.L., Mo, J.X., Lai, C.L. and Lai, M.H. (2023), "Seismic performance of a ring beam joint connecting FTCES column and RC/ESRC beam with NSC", *J. Build. Eng.*, 105366. https://doi.org/10.1016/j.jobe.2022.105366
Shaw, A.D., Gatti, G., Gonçalves, P.J.P., Tang, B. and Brennan, M.J. (2021), "Design and test of an adjustable quasi-zero stiffness device and its use to suspend masses on a multi-modal structure", *Mech. Syst. Signal Process.*, **152**, 107354. https://doi.org/10.1016/j.ymssp.2020.107354
Shi, Y., Luo, Z., Zhou, X., Xue, X. and Li, J. (2022), "Post-fire mechanical properties of titanium–clad bimetallic steel in different cooling approaches", *J. Constr. Steel Res.*, **191**, 107169. https://doi.org/10.1016/j.jcsr.2022.107169
Shi, Y., Wang, J., Zhou, X. and Xue, X. (2023), "Post-fire properties of stainless – clad bimetallic steel produced by explosive welding process", *J. Constr. Steel Res.*, **201**, 107690. https://doi.org/10.1016/j.jcsr.2022.107690
Valeev, A., Tashbulatov, R. and Mastobaev, B. (2021), "Designing and experimental study of compact vibration isolator with quasi-zero stiffness", *Struct. Eng. Mech., Int. J.*, **79**(4), 415-428. https://doi.org/10.12989/sem.2021.79.4.415
Wang, Y. and Jing, X.J. (2019), "Nonlinear stiffness and dynamical response characteristics of an asymmetric X-shaped structure", *Mech. Syst. Signal Process.*, **125**, 142-169.

https://doi.org/10.1016/j.ymssp.2018.03.045
Wang, K., Zhou, J.X., Chang, Y.P., Ouyang, H.J., Xu, D.L. and Yang, Y. (2020a), "A nonlinear ultra-low-frequency vibration isolator with dual quasi-zero-stiffness mechanism", *Nonlinear Dyn*., **101**(2), 755-773. https://doi.org/10.1007/s11071-020-05806-0
Wang, L., Zhang, Y.W., Ho, J.C.M. and Lai, M.H. (2020b), "Fatigue behaviour of composite sandwich beams strengthened with GFRP stiffeners", *Eng. Struct*., **214**, 110596. https://doi.org/10.1016/j.engstruct.2020.110596
Wang, Q., Zhou, J.X., Xu, D.L. and Ouyang, H.J. (2020c), "Design and experimental investigation of ultra-low frequency vibration isolation during neonatal transport", *Mech. Syst. Signal Process*., **139**, 106633. https://doi.org/10.1016/j.ymssp.2020.106633
Wang, K., Zhou, J.X., Ouyang, H.J., Chang, Y.P. and Xu, D.L. (2021), "A dual quasi-zero-stiffness sliding-mode triboelectric nanogenerator for harvesting ultralow-low frequency vibration energy", *Mech. Syst. Signal Process*., **151**, 107368. https://doi.org/10.1016/j.ymssp.2020.107368
Wang, L., Sun, J., Ding, T., Liang, Y., Ho, J.C.M. and Lai, M.H. (2022), "Manufacture and behaviour of innovative 3D printed auxetic composite panels subjected to low-velocity impact load", *Structures*, **38**, 910-933. https://doi.org/10.1016/j.istruc.2022.02.033
Wu, W.J., Chen, X.D. and Shan, Y.H. (2014), "Analysis and experiment of a vibration isolator using a novel magnetic spring with negative stiffness", *J. Sound Vib*., **333**(13), 2958-2970. https://doi.org/10.1016/j.jsv.2014.02.009
Wu, Z., Jing, X.J., Bian, J., Li, F.M. and Allen, R. (2015), "Vibration isolation by exploring bio-inspired structural nonlinearity", *Bioinspir. Biomim*., **10**(5), 056015. https://doi.org/10.1088/1748-3190/10/5/056015
Xu, D.L., Yu, Q.P., Zhou, J.X. and Bishop, S.R. (2013), "Theoretical and experimental analyses of a nonlinear magnetic vibration isolator with quasi-zero-stiffness characteristic", *J. Sound Vib*., **332**(14), 3377-3389. https://doi.org/10.1016/j.jsv.2013.01.034
Yam, M.C.H., Ke, K., Lam, A.C.C. and Zhao, Q. (2019), "Performance of single-coped beam with slender web and quantification of local web buckling strength", *Thin-Wall. Struct*., **144**, 106355. https://doi.org/10.1016/j.tws.2019.106355
Yam, M.C.H., Ke, K., Huang, Y., Zhou, X.H. and Liu, Y.C. (2022), "A study of hybrid self-centring beam-to-beam connections equipped with shape-memory-alloy-plates and washers", *J. Constr. Steel Res*., **198**, 107526. https://doi.org/10.1016/j.jcsr.2022.107526
Yan, G., Zou, H.X., Wang, S., Zhao, L.C. and Wu, Z.Y. (2022), "Bio-inspired toe-like structure for low-frequency vibration isolation", *Mech. Syst. Signal Process*., **162**, 108010. https://doi.org/10.1016/j.ymssp.2021.108010
Yang, T., Cao, Q.J. and Hao, Z.F. (2021), "A novel nonlinear mechanical oscillator and its application in vibration isolation and energy harvesting", *Mech. Syst. Signal Process*, **155**, 107636. https://doi.org/10.1016/j.ymssp.2021.107636
Yao, Y.H., Li, H.G., Li, Y. and Wang, X.J. (2020), "Analytical and experimental investigation of a high-static-low-dynamic stiffness isolator with cam-roller-spring mechanism", *Int. J. Mech. Sci*., **186**, 105888. https://doi.org/10.1016/j.ijmecsci.2020.105888
Ye, K., Ji, J.C. and Brown, T. (2020), "Design of a quasi-zero stiffness isolation system for supporting different loads", *J. Sound Vib*., **471**, 115198. https://doi.org/10.1016/j.jsv.2020.115198
Yi, S., Chen, M.T. and Young, B. (2023), "Design of concrete-filled cold-formed steel elliptical stub columns", *Eng. Struct*., **276**, 115269. https://doi.org/10.1016/j.engstruct.2022.115269
Zhang, R., Wang, W. and Ke, K. (2020), "Quantification of seismic demands of damage-control tension-only concentrically braced steel beam-through frames (TCBSBFs) subjected to near-fault ground motions based on the energy factor", *Soil Dyn. Earthq. Eng*., **129**, 105910. https://doi.org/10.1016/j.soildyn.2019.105910
Zhang, P., Yam, M. C.H., Ke, K., Zhou, X.H. and Chen, Y. (2022), "Steel moment resisting frames with energy-dissipation rocking columns under near-fault earthquakes: Probabilistic performance-based-plastic-design for the ultimate stage", *J. Build. Eng*., **54**, 104625. https://doi.org/10.1016/j.jobe.2022.104625
Zhang, H., Zhou, X.H., Ke, K., Yam, M.C.H., He, X. and Li, H. (2023), "Self-centring hybrid-steel-frames employing energy dissipation sequences: Insights and inelastic seismic demand model", *J. Build. Eng*., **63**, 105451. https://doi.org/10.1016/j.jobe.2022.105451
Zhao, F., Ji, J.C., Ye, K. and Luo, Q.T. (2020), "Increase of quasi-zero stiffness region using two pairs of oblique springs", *Mech. Syst. Signal Process*., **144**, 106975. https://doi.org/10.1016/j.ymssp.2020.106975
Zheng, Y.S., Zhang, X.N., Luo, Y.J., Zhang, Y.H. and Xie, S.L. (2018), "Analytical study of a quasi-zero stiffness coupling using a torsion magnetic spring with negative stiffness", *Mech. Syst. Signal Process*., **100**, 135-151. https://doi.org/10.1016/j.ymssp.2017.07.028
Zhong, R.M., Zong, Z.H., Pai, P.F. and Ruan, X.W. (2019), "Multi-stopband negative stiffness composite column design for vibration absorption", *Thin-Wall. Struct*., **144**, 106330. https://doi.org/10.1016/j.tws.2019.106330
Zhou, X.H., Zhang, H., Ke, K., Guo, L. and Yam, M.C.H. (2021a), "Damage-control steel frames equipped with SMA connections and ductile links subjected to near-field earthquake motions: A spectral energy factor model", *Eng. Struct*., **239**, 112301. https://doi.org/10.1016/j.engstruct.2021.112301
Zhou, X.H., Ke, K., Yam, M.C.H., Zhao, Q., Huang, Y. and Di, J. (2021b), "Shape memory alloy plates: Cyclic tension-release performance, seismic applications in beam-to-column connections and a structural seismic demand perspective", *Thin-Wall. Struct*., **167**, 108158. https://doi.org/10.1016/j.tws.2021.108158
Zhou, S.H., Liu, Y.L., Jiang, Z.Y. and Ren, Z.H. (2022a), "Nonlinear dynamic behavior of a bio-inspired embedded X-shaped vibration isolation system", *Nonlinear Dyn*., **110**, 153-175. https://doi.org/10.1007/s11071-022-07610-4
Zhou, X.H., Chen, Y., Ke, K., Yam, M.C.H. and Li, H. (2022b), "Hybrid steel staggered truss frame (SSTF): A probabilistic spectral energy modification coefficient surface model for damage-control evaluation and performance insights", *J. Build. Eng*., **45**, 103556. https://doi.org/10.1016/j.jobe.2021.103556
Zhou, Z., Ke, K., Chen, Y. and Yam, M.C.H. (2022c), "High strength steel frames with curved knee braces: performance-based damage-control design framework", *J. Constr. Steel Res*., **196**, 107392. https://doi.org/10.1016/j.jcsr.2022.107392
Zhou, X.H., Tan, Y.C., Ke, K., Yam, M.C.H., Zhang, H.Y. and Xu, J.Y. (2023), "An experimental and numerical study of brace-type long double C-section steel slit dampers", *J. Build. Eng*., **64**, 105555. https://doi.org/10.1016/j.jobe.2022.105555
Zou, D.L., Liu, G.Y., Rao, Z.S., Tan, T., Zhang, W.M. and Liao, W.H. (2021), "A device capable of customizing nonlinear forces for vibration energy harvesting, vibration isolation, and nonlinear energy sink", *Mech. Syst. Signal Process*., **147**, 107101. https://doi.org/10.1016/j.ymssp.2020.107101